JOURNAL OF COASTAL AND HYDRAULIC STRUCTURES

Vol. 4, 2024, 34

Analytical and Numerical Modelling of Debris Impact Events on Columns

Patrick Joynt[1], Ioan Nistor [1], Dan Palermo [2], and Jacob Stolle [3]

[1]pjoyn059@uottawa.ca, inistor@uottawa.ca, University of Ottawa, Ottawa, Canada
[2]dan.palermo@lassonde.yorku.ca, York University, Lassonde School of Engineering, Toronto, Canada
[3]Jacob.Stolle@ete.inrs.ca, Institut National de la Recherche Scientifique, Quebec, Canada

Research Article. **Submitted:** 12 March 2023. **Reviewed:** 7 February 2024. **Accepted** after double-anonymous review: 7 April 2024. **Published:** 27 May 2024.

DOI: https://doi.org/10.59490/jchs.2024.0034

Cite as: "Joynt, P., Nistor, I. ., Palermo, D. ., & Stolle, J. (2024) Analytical and Numerical Modelling of Debris Impact Events on Columns. *Journal of Coastal and Hydraulic Structures, 4,* p.34, https://doi.org/10.59490/jchs.2024.0034 ".

This paper is part of the **Thematic Series** of selected papers on **Debris Hazards in a Coastal Context**. The series addresses the potential effects of debris on hazards in coastal and estuarine environments, like direct damage to coastal infrastructure, influence on hydraulic loading, and contribution to pollution. Series editors: Jacob Stolle & Ioan Nistor.

ISSN: 2667-047X online

Abstract

Post-disaster surveys of tsunamis have emphasized the need for an in-depth understanding of debris loading. Until now, empirical formulas used to estimate debris impact loads are based on single-degree-of-freedom (SDOF) models. However, the validity of these SDOF models to estimate debris impact loads has not been studied extensively. This study investigates the validity of using a SDOF model to predict debris impact forces by comparing its force response to experimental data and a multiple-degree-of-freedom (MDOF) model developed. Additionally, a comparative analysis was conducted to assess the provisions on debris impact loads in Chapter 6 of ASCE 7-22 against these alternative methods. The MDOF method was shown to model accurately the experimental force response data, while all other methods for estimating debris impact loads overestimated the force response in both magnitude and frequency. Furthermore, the impact loads generated by the MDOF model proved to be longer in duration but smaller in magnitude than loads generated using the SDOF model and Chapter 6 of ASCE 7-22.

In addition, a performant numerical model was developed to simulate single and multi-debris transport and impact loads on a column. The dynamic numerical model was developed within the general-purpose finite element program LS-DYNA. Inside this modelling framework, the Arbitrary Lagrangian-Eulerian (ALE) method was used to simulate dam-break wave generated debris impact loads onto the column. The model accurately replicated the water surface elevations, hydrodynamic forces, debris transport, and debris impact forces presented in Stolle et al. (2019) and Stolle et al. (2020b). The model's ability to simulate debris impact events demonstrates its potential as a valuable tool for designing and evaluating critical infrastructure's resilience against extreme coastal inundation events, such as tsunamis.

Keywords

Debris-impact, Dam break wave, Impact force estimation, Extreme events, Structural response, Numerical modelling

1 Introduction

Recent devastation caused by extreme coastal inundation events, such as the 2010 tsunami in Chile, the 2011 Tohoku tsunami in Japan, and the 2018 Indonesian tsunami, have increased awareness about the effectiveness of design codes used to estimate loads generated during such extreme events. ASCE/SEI 7-22 Chapter 6 classifies tsunami loads into the following categories:

- Hydrostatic load – a load applied onto a structure due to a standing mass of water.
- Hydrodynamic load – a load applied onto a structure due to water flowing against or around it.
- Impact load – a load applied onto a structure due to debris or other objects being transported by the design tsunami and striking the structure.

From post-tsunami surveys, each of these loading conditions can be seen to have caused extensive damage to coastal communities (Naito et al. 2014, Syamsidik et al. 2019). Specifically, during the 2018 Indonesian tsunami the damage caused by debris impacts was seen in most of the inundated areas (Syamsidik et al. 2019), highlighting the importance of understanding these types of loads for structural design. Palermo et al. (2012) presented specific examples of structural damage experienced during the 2010 tsunami in Chile and the 2011 Tohoku tsunami. These damages range from local member failure to global structural damage as shown in Figure 1.

Figure 1: Global (left) and local (right) structural damage (Palermo et al. 2012).

Stolle et al. (2020a) present further examples of structural damage due to various types of debris impacts during the 2018 Indonesian tsunami. Stolle et al. (2020a) show that debris impacts can be due to a wide range of debris types, such as concrete debris and ships as shown in Figure 2. However, it is important to note that debris sources can encompass anything that is being transported by the tsunami. Additionally, the damage caused by debris impacts can vary widely; Stolle et al. (2020a) show that structural damage can range from concrete spalling to complete failure of exterior columns, as shown in Figure 2.

Figure 2: Concrete debris impacts (left) and vessel impacts (right) (photos taken by Jacob Stolle).

From post-tsunami field studies, it is evident that an important design consideration for tsunami-resilient infrastructure is debris impact loading. This type of loading has seen more attention in recent history, however, the complexity of the processes involved require new approaches and more detailed studies.

2 Literature Review and Objectives

2.1 Literature Review of Debris Impact Models

Debris impact loads can be generated by debris damming, single debris impacts, and multi-debris impacts. Additionally, multi-debris impacts can be separated into two categories, the first being simultaneous impacts and the second being asynchronous impacts (Stolle et al. 2020b). This study will focus on two aspects:

1. Analytical analysis of single debris impacts, for which there have been several design guidelines developed, such as Chapter 6 of ASCE 7-22 and FEMA P-646 (FEMA 2012).
2. Numerical modelling of single and multi-debris impact events using fully 3D coupled fluid-structure interaction.

There have been several formulations to analytically express single debris impact loads that are based on the analytical solution to the one-dimensional wave equation (Aghl et al. 2014; Aghl et al. 2015; Riggs et al. 2013; Stolle et al. 2018b), a two-degree of freedom (2DOF) model (Stolle et al. 2019), or a model based on Hertzian contact mechanics (Ikeno et al. 2016). The approach taken in ASCE 7-22 is derived from Haehnel and Daly (2004), who investigated large woody debris impacts on structures. Haehnel and Daly (2004) determined through experimental analysis that the maximum impact force during flooding events can be estimated by a single-degree-of-freedom (SDOF) model with a contact-stiffness approach. Haehnel and Daly (2004) defined the maximum impact force (F) as a function of the impact velocity (u), mass of the debris (m_d), and the debris stiffness (k_d):

$$F = u\sqrt{m_d k_d} \quad [1]$$

In the study conducted by Haehnel and Daly (2004), the structure being impacted was assumed to be completely rigid, the debris was assumed to remain within its elastic capacity, and the influence of damping on the response was considered negligible. The assumption that a structure remains completely rigid during an impact event implies that there is no deformation in the structure, which is an unrealistic assumption based on post-tsunami field surveys (Naito et al. 2014; Stolle et al. 2020a). Haehnel and Daly (2004) modified Eq. [1] to include the influence of the contact stiffness between the debris and structure. The effective stiffness of the collision (k) is a function of the structure stiffness (k_s) and the debris stiffness as shown below:

$$\frac{1}{k} = \frac{1}{k_s} + \frac{1}{k_d} \quad [2]$$

The approach taken by Chapter 6 Clause 6.11.2 of ASCE 7-22 to calculate the impact force for wooden logs, poles, and shipping containers is the same as Eq. [1]. However, the stiffness term is defined as the lesser of the effective stiffness of the impact debris or the lateral stiffness of the impacted structural elements deformed by the impact. Additionally, the standard also applies two scale factors to the impact force that are related to the importance factor of the building (I_{tsu}) and the orientation coefficient (C_0). The orientation coefficient echoes the conclusion from Haehnel and Daly (2004), who note that impact geometry has an influence on the impact force. Clause 6.11.2 of ASCE 7-22 specifies the impact duration (t_d) for logs and poles as a function of the mass of the debris, maximum flow velocity (u_{max}), and the impact force:

$$t_d = \frac{2 m_d u_{max}}{F} \quad [3]$$

Matsutomi (2009) presented a formula that estimated the collision force for driftwood entrained in inundating flow. The author experimentally studied the in-water impact force induced by small-scale driftwood impacting a rigid structure. The author noted that the added mass of the displaced fluid by the driftwood needs to be accounted for in the force equation, as this volume of water is decelerated along with the driftwood when the impact occurs. He proposed a force equation as a function of the unit weight of the debris (γ_d), the diameter of the driftwood (D_w), the length of the driftwood

(L_w), the debris collision velocity (v_{A0}), the yield stress of the driftwood (σ_{df}), gravity (g), and the added mass coefficient (C_{MA}):

$$F = 1.6C_{MA}\left(\frac{v_{A0}}{\sqrt{gD_w}}\right)^{1.2}\left(\frac{\sigma_{df}}{\gamma_d L_w}\right)^{0.4}(\gamma_d D_w^2 L_w) \quad [4]$$

Ikeno et al. (2013) also presented a formula based on Hertzian contact mechanics, that estimated the collision force for woody debris. The formula was validated by in-air and in-water physical experiments:

$$F = \kappa(C_{MA}m)^{0.6}V_H^{1.2}D^{0.2}\tilde{E}^{0.4} \quad [5]$$

Where κ = dimensionless coefficient equal to 0.243, C_{MA} = added mass of the fluid, V_H = collision speed of the debris, D = diameter of the debris, and $\tilde{E}$ = effective Young's modulus. Ikeno et al. (2016) modified the debris impact formula outlined in Ikeno et al. (2013) to include the influence of the debris collision angle.

2.2 Objectives, Methodology, and Research Significance

Most of the aforementioned studies for estimating debris impact loads have developed debris impact force equations based on the assumption that the impact event can be treated as a SDOF system. The first objective of this study is to provide a comparative analysis on how different methods estimate debris impact loads and how these methods influence the force response of a column. The three methods that will be investigated are a SDOF method, a MDOF method, and Chapter 6 of ASCE 7-22. This comparative analysis reveals how ASCE 7-22 holds up against alternative methods for estimating debris impact loads.

The second objective of this study is to numerically simulate dam-break wave generated debris impact events using a fully 3D coupled fluid-structure interaction (FSI) in the general-purpose finite element program LS-DYNA. Previous literature has focused on quantifying tsunami generated debris impact loads through scaled-down experimental studies (see Matsutomi (2009), Ko et al. (2015), Stolle et al. (2019)) or full-scale experimental and numerical studies that do not include the hydrodynamics associated with tsunami generated debris impacts (see Aghl et al. (2014), Aghl et al. (2015)). The aim of this study is to understand the capabilities of numerical models to simulate dam-break wave generated debris impact events by comparing the model to experimental data.

3 Methods for Estimating Debris Impact Force Histories

3.1 Description of Experimental Data

The experimental data analyzed in this study was obtained from Stolle et al. (2019), who carried out the experimental program in the Hydraulics Laboratory at the University of Ottawa. The facility houses a dam-break wave flume with a length of 30 m, a width of 1.5 m, and a maximum impoundment depth up to 0.7 m. The reservoir of water has a length of 21.55 m, which was impounded behind a swing-gate at various inundation depths for the experimental study. Figure 3 outlines a schematic of the dam-break wave flume at the University of Ottawa.

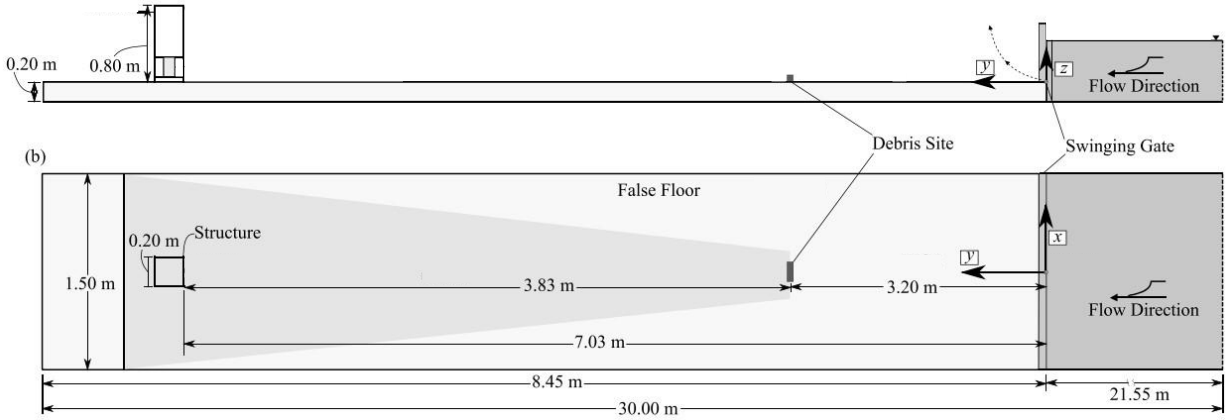

Figure 3: Dam-break flume at the University of Ottawa (modified from Stolle et al. 2019)

The experimental program consisted of a structural column subjected to dam-break wave generated debris impact events. The debris used in the experimental study were 1:40 geometrically scaled 20-foot shipping containers constructed of positively buoyant polyethylene with dimensions of 0.06 x 0.06 x 0.15 m, a wall thickness of 0.005 m, and a mass of 0.236 kg. The structure used in the experimental study had a square hollow cross-section construction from acrylic with dimensions of 0.20 x 0.20 x 0.80 m and a wall thickness of 0.005 m. From the experimental study, the modulus of elasticity of the structure was determined to be 2.50 GPa. Other parameters required for the numerical modelling of the structure were obtained from the ANSYS GRANTA material selector (ANSYS 2018). The mass density of the structure was assumed to be 1200 kg/m^3 with a Poisson's ratio of 0.375 for an acrylic structure, and the shear coefficient was assumed to be equal to 0.50 for a thin-walled hollow cross-section. The experimental program recorded the water surface elevation of the dam-break wave, the force response of the structure due to the combined wave and debris impact, and the debris impact velocity.

Stolle et al. (2019) processed the force response data signal of the structure to remove components associated with instrument noise and hydrodynamic loads using the Ensemble Empirical Mode Decomposition (EEMD) method (Huang et al. 1998). The filtered signal represents the structural response only attributed to the debris impact load. Further information on the experimental program can be found in Stolle et al. (2019).

In this study, 22 experiments were selected from the experimental data set. The selection involved removing experiments with bad data, which was defined as experiments where the force response signal data did not present any obvious impact event (i.e. no peaks in the signal). Secondly, experiments where multiple impacts occurred in a short period of time were removed, as the goal was to extract the initial impact force and not impact forces due to high frequency pounding events. Finally, only single-debris impact events generated from an inundation depth of 0.40 m were considered.

3.2 Analytical Models

3.2.1 Single-Degree-of-Freedom Model

Duhamel's integral was used to resolve the force response history (R(t)) of a SDOF system subjected to an arbitrary forcing function (Chopra 2017). Duhamel's integral is a function of the stiffness of the structure (k), the mass of the structure (m_s), the damping coefficient (ξ), the damped and undamped natural circular frequency of the structure (ω_d, ω_n), the time elapsed since impact (τ), time (t), and the impact loading history (p(τ)) (Chopra 2017):

$$R(t) = \frac{k}{m_s \omega_d} \int_0^t p(\tau) e^{-\xi \omega_n (t-\tau)} \sin \omega_d (t-\tau)\ d\tau \quad [6]$$

The solution follows an iterative procedure where the integral is evaluated by using an incremental summation over time as outlined in Navaratnam et al. (2013). The force response was fit to the experimental force response data by minimizing the difference between the measured and modelled data. This was achieved by iteratively estimating the impact magnitude, impact duration, damping coefficient, structural stiffness, and natural frequency of the structure;

additional information on the fitting process can be found in Joynt et al. (2021). The impact loading history took the form of a half-sine pulse, as full-scale shipping container impacts suggested the impact history has a similar shape to a half-sine (Aghl et al. 2014).

Stolle et al. (2019) stated that the natural frequency of the structure was measured as 70 Hz (± 2.2 Hz). Stolle et al. (2019) also stated that the stiffness of the structure was estimated to be 4.685 x 10^5 N/m with lower and upper bounds of 4.653 x 10^5 N/m and 4.701 x 10^5 N/m. These values provided upper and lower bounds for both the natural frequency and the structural stiffness within the fitting algorithm. Stolle et al. (2019) also estimated a damping coefficient of 0.045. However, the water depth around the structure can influence the damping of the structural response (Oumeraci et al. 1993) and hence, an error bar of ± 0.005 was assumed.

3.2.2 Multiple-Degree-of-Freedom Model

Newmark's constant average acceleration method was used to resolve the force response history of the column modelled as a MDOF system subjected to an arbitrary forcing function (Chopra 2017). This was done by solving the equation of motion in the time domain. The equation of motion is a function of the mass matrix ([m]), damping matrix ([c]), stiffness matrix ([k]), acceleration vector ($\{\ddot{x}\}$), velocity vector ($\{\dot{x}\}$), displacement vector ($\{x\}$), and the forcing function (p(t)):

$$[m]\{\ddot{x}\} + [c]\{\dot{x}\} + [k]\{x\} = \{p(t)\} \quad [7]$$

The structure in Stolle et al. (2019) was chosen to be modelled as a cantilevered column constructed of 160 elastic beam elements using a time step of $1e^{-6}$ s based on results from a mesh and time step sensitivity analysis (Joynt et al. 2021).

The stiffness matrix was derived from the direct stiffness method using Timoshenko's beam theory, as Khowitar et al. (2014) demonstrated that shear behavior dominates the initial response of a pole impacting a column. The mass matrix was derived using a consistent mass matrix and the damping matrix was derived from Rayleigh damping. Following the development of the mass, stiffness, and damping matrices, a similar fitting procedure to that outlined in the SDOF method was followed. The model shear response time history was fit to the experimental force response data by minimizing the difference between the measured and modelled data; more information on the fitting process can be found in Joynt et al. (2021). For the MDOF analysis, this fitting was completed by varying the peak impact force and duration. The mass, stiffness, and damping matrices were held constant. The location of the impact force along the beam was determined from the water surface elevation at the face of the structure. The impact locations varied from 0.16 m to 0.50 m with an average location of 0.40 m above the base of the structure. As outlined in the SDOF method, the impact loading history took the form of a half-sine pulse.

3.2.3 Analytical Model

The analytical model follows the formulas and procedures outlined in Clause 6.11.2 and 6.11.8 of ASCE 7-22 to determine the impact magnitude, duration, and shape. The impact force and duration are functions of the importance factor, orientation coefficient, maximum flow velocity, the lesser of the effective stiffness of the impact debris or lateral stiffness of the impacted structural element, and the mass of the debris:

$$F_i = I_{tsu} C_0 F_{ni} \quad [8]$$

$$F_{ni} = u_{max}\sqrt{k m_d} \quad [9]$$

$$t_d = \frac{2 m_d u_{max}}{F_{ni}} \quad [10]$$

For this analysis, the importance factor was selected to be one, corresponding to a Tsunami Risk Category of II and following Clause 6.11.6, the orientation is equal to 0.65 for shipping containers. Additionally, following Clause 6.11.8, the impact force history will take the shape of a rectangular pulse with a magnitude defined by Eq. [8] and duration defined by Eq. [10].

3.3 Results and Discussion

This section presents and discusses the debris impact force histories generated for each method and how these debris impact force histories influence the force response of the column. Figure 4 presents the fitting results from the SDOF and MDOF models for one of the experimental force response time histories from the experimental data set. Figure 4 demonstrates that the SDOF fit resulted in a force response that is in phase with the experimental data. Furthermore, after the initial peak of the force response, the SDOF model captured the magnitude of the subsequent peaks but underestimated the maximum measured force by 40%. Additionally, the SDOF model was not able to capture the dual peak behavior of the in the initial response, as this behavior is associated with higher mode effects which can only be captured by modelling more than one degree of freedom.

Similar to the SDOF fitting model, the MDOF fitting model results in a force response that is in phase with the measured data. However, the MDOF model captured all peaks of the measured response and underestimated the maximum measured force by 8.7%. Additionally, the MDOF model captured the dual peak behavior present in the initial response, as the MDOF model allows for higher mode responses to be captured. Both models were able to capture the general response of the system, however, the MDOF model performed better at capturing the maximum measured force response and the higher mode effects.

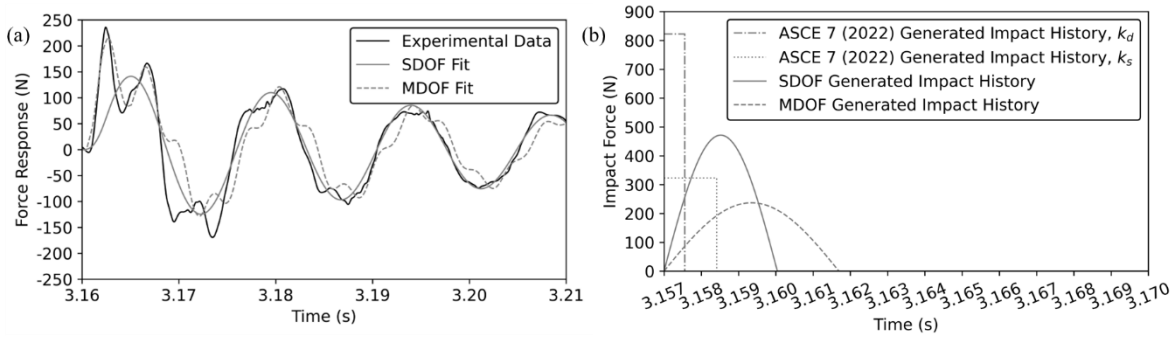

Figure 4: (a) SDOF and MDOF fitting methods compared to one experimental data point and (b) impact force histories derived from the fitting methods and ASCE 7-22.

After fitting the SDOF and MDOF models to the force response curve, the impact forces that generated the responses in Figure 4(a) were extracted, these are presented in Figure 4(b). For the force response history shown in Figure 4(a), the measured impact velocity was 1.50 m/s and using the debris and structure stiffnesses, two impact force histories were generated following ASCE 7-22 as shown in Figure 4(b). Table 1 outlines the impact magnitude, duration, and impulse for each of the impact histories shown in Figure 4(b).

Table 1: Impact force history properties associated with Figure 4(b).

Method	Magnitude (N)	Duration (s)	Impulse (N-s)
ASCE 7-22 using k_d^*	822.34	0.0006	0.46
ASCE 7-22 using k_s^*	322.83	0.0014	0.46
SDOF	471.49	0.0030	0.91
MDOF	236.93	0.0047	0.71

*Stolle et al. (2019) outline k_d and k_s used in this analysis.

From Figure 4(b) and Table 1, it can be observed that using either debris or structure stiffness in the debris impact formulation results in a significantly different impact history. This highlights the importance of the stiffness parameter when calculating the impact magnitude and duration as per Clause 6.11.2 of ASCE 7-22. Applying these impact force histories to the MDOF model results in the force responses outlined in Figure 5.

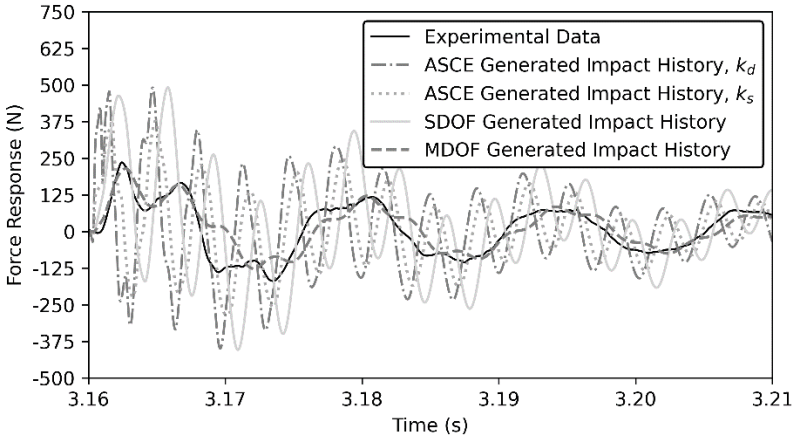

Figure 5: Force response for all methods for one experimental data point.

From Figure 5, only the MDOF model for generating the impact force history resulted in a response that models the experimental data accurately both in frequency and in magnitude. Additionally, only the MDOF model could capture the dual peak behavior present in the initial response. All other methods overestimated the frequency and magnitude of the measured response.

Extending this analysis to all 22 experimental force response time histories, a suite of impact curves can be generated for each method as shown in Figure 6. Figures 6(a) and 6(b) present the impact curves generated by following ASCE 7-22. Figures 6(c) and 6(d) present the impact curves generated by the SDOF and MDOF fitting models.

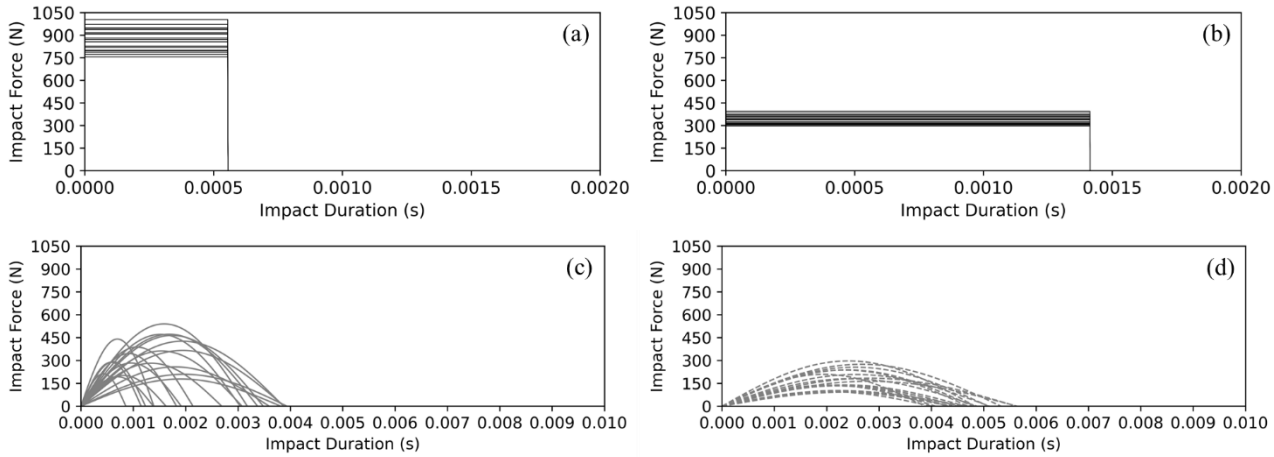

Figure 6: (a) ASCE 7-22 method using k_d, (b) ASCE 7-22 method using k_s, (c) SDOF model, (d) MDOF model.

Table 2 outlines the mean and standard deviation of the impact magnitude, duration, and total impulse for each set of impact force history curves.

Table 2: Statistics for each impact force history suite.

Method	Magnitude (N)		Duration (s)		Impulse (N-s)	
	Mean	Std.	Mean	Std.	Mean	Std.
ASCE 7-22 using k_d	875.25	70.22	0.0006	0.0000	0.49	0.04
ASCE 7-22 using k_s	343.60	27.57	0.0014	0.0000	0.49	0.04
SDOF	333.96	106.94	0.0026	0.0010	0.57	0.32
MDOF	171.07	62.91	0.0047	0.0005	0.52	0.22

Observing Figure 6 and Table 2, the impact force history suites developed using ASCE 7-22 resulted in no variation in the impact durations, as the impact velocity does not influence the impact duration based on the formula in the standard.

Additionally, the stiffness value used in Clause 6.11.2 of ASCE 7-22 has a significant influence on the impact magnitudes and durations. However, regardless of the type of stiffness value chosen, the total impulse into the system will be the same when developing impact force histories by following Clauses 6.11.2 and 6.11.8 of ASCE 7-22. Comparing the impact force history suites developed using the SDOF and MDOF fitting models, it is apparent that the SDOF model resulted in a wider range of impact magnitudes and durations when compared to the MDOF model.

Using the impact force histories outlined in Figure 6 as input into the MDOF model, the maximum modelled force response can be directly compared to the maximum measured force response as shown in Figure 7.

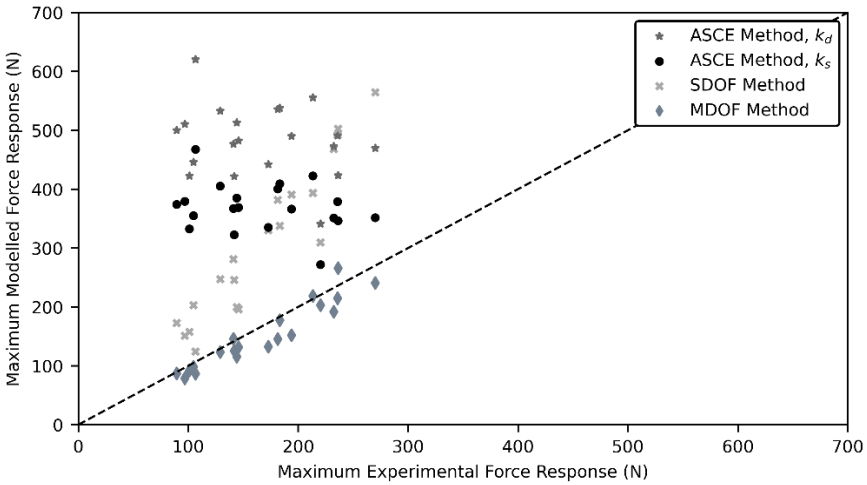

Figure 7: Maximum experimental force response versus maximum modelled force response.

Observing Figure 7, the dashed line represents the 1:1 ratio line which corresponds to when the maximum modelled shear force at the force transducer location is equal to the maximum experimental force response. From Figure 7, the maximum modelled force responses resulting from the impact histories developed by the SDOF fitting model show a large range in variability which is directly correlated to the variability of the impact force histories shown in Figure 6(c). For example, using the SDOF fitting method resulted in events that induced a maximum modelled force response at both 300 N and 500 N while the measured maximum force is 225 N. This result indicates that even though the SDOF system subjected to the impact history may provide a response that is in general agreement with the measured data, when that same impact force history is applied to a MDOF system, the impact force no longer results in a realistic response. This is evident in Figure 7 as the scatter associated with the SDOF model falls far from the 1:1 line. Consequently, the maximum modelled force responses developed in the MDOF model using the impact histories generated from the SDOF fitting method do not accurately represent the maximum experimental force responses. The SDOF model for estimating impact histories resulted in a maximum force response that is, on average, 1.8 times larger than the maximum measured force response. However, the range of values for this ratio is between 1.2 to 2.1. Furthermore, as the maximum measured force response increases, the amount that the SDOF model overestimates the measured force also increases. This suggests that as impact force histories increase in magnitude, the validity of using a SDOF model to estimate the debris impact force decreases.

Examining the maximum modeled force responses generated by the MDOF fitting model, it can be concluded that the MDOF fitting model provides a reliable estimate of the maximum measured force responses. This is evident in Figure 7, as the scatter associated with the MDOF model is in close proximity to the 1:1 line, indicating that the model accurately estimates impact force histories. On average, the MDOF model underestimated the maximum measured force response, with a ratio of 0.9 between the maximum modeled and maximum measured force responses. However, it is worth noting that the ratio ranges from 0.8 to 1.1 times the maximum measured force response, suggesting that the degree of underestimation may vary based on the specific impact scenario.

Figure 7 also presents the maximum force responses induced by the impact histories developed following Clauses 6.11.2 and 6.11.8 of ASCE 7-22. It is apparent from the plot that regardless of the stiffness value chosen, the maximum force response using the methods outlined in ASCE 7-22 resulted in an upper-bound estimation of the maximum measured force response. When the debris stiffness is used, the maximum modelled force responses are larger than when the

structure stiffness is used, as the debris stiffness is larger than the structure stiffness. On average, when the structure stiffness is used, the maximum modelled force response is 2.5 times larger than the measured value. This ratio ranges from a minimum of 1.2 to a maximum of 4.4. When the debris stiffness is used, this value increases to an average of 1.3 and ranges from a minimum of 1.5 to a maximum of 5.8.

4 Numerical Modelling of Dam-Break Wave Generated Debris Impact Events

4.1 Description of Numerical Model

The numerical model was developed within the general-purpose finite element program LS-DYNA. Inside this modelling framework, the ALE method was used to simulate both single and multi-debris dam-break wave generated impact loads onto a column. An ALE time step as described in Hallquist (2006) first performs a Lagrangian time step where the mesh follows the material deformation, then an advection step is performed where the model decides which nodes to move, moves the boundary nodes, moves the interior nodes, calculates the transport of element-centered variables, and calculates the momentum transport and updates the velocities. Further details of the ALE method can be found in Joynt et al. (2021). For this study, the structure and debris were simulated using the FEM approach and the fluid was modelled using the FVM approach, for which FSI was modelled by coupling the points at the interface between the FEM and FVM meshes.

4.1.1 Computational Domain

As described previously, this study uses the physical modelling work by Stolle et al. (2019) and Stolle et al. (2020b) who performed the experimental program in the Hydraulics Laboratory at the University of Ottawa. For the numerical modelling presented in this study, only the results associated with an impoundment depth of 0.40 m are used. Figure 8 outlines a schematic of the dam-break wave flume at the University of Ottawa. Key parameters that were measured during the experimental program are the water surface elevations at wave gauges (WG1 – WG4), the force response of the structure due to combined wave and debris impact, debris transport paths, and debris impact velocities.

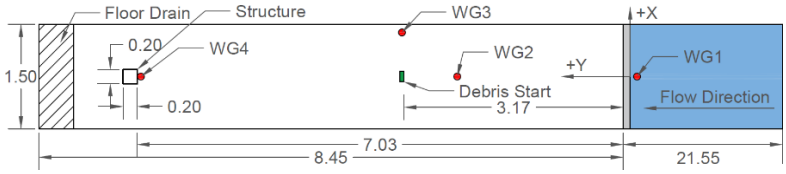

Figure 8: Schematic of the University of Ottawa Dam-Break Wave Flume (Units in Meters).

The dam-break wave flume was recreated in LS-DYNA and is shown in Figure 9(a). Note that the length of the reservoir in the numerical model is not equal to the length of the reservoir used in the physical model. This is because the debris impact events were over after six seconds from releasing the wave and sensitivity testing showed that the water surface elevation at WG1 was held constant after six seconds with a reservoir length of 10 m (see Joynt et al. 2021 for more details). Figure 9(b) also outlines an example debris layout.

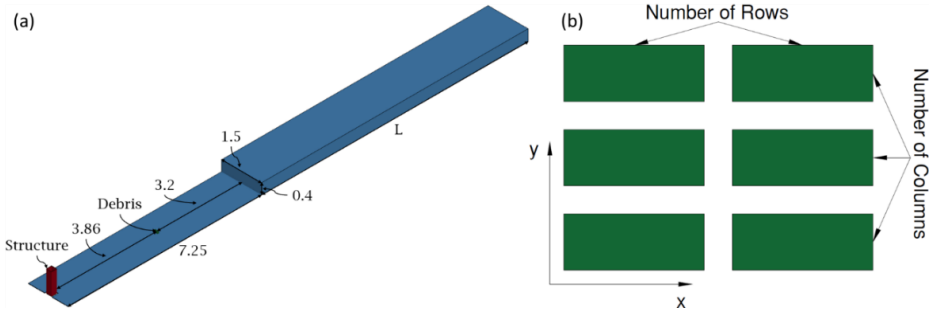

Figure 9: (a) University of Ottawa Dam-Break Wave Flume in LS-DYNA (Units in Meters). (b) Example Debris Layout

4.1.2 Mesh Sensitivity Analysis

Mesh sensitivity analysis was completed to investigate how sensitive the hydrodynamics of the simulation are to mesh refinement. As such, the debris was not modelled during this sensitivity testing. The parameters that were investigated during the mesh sensitivity analysis were the water surface elevations at the wave gauges and the hydrodynamic force on the structure. The numerical modelling results are compared to the experimental data of Stolle et al. (2019) and the water surface elevation is also compared to the analytical expression of a dam-break wave outlined in Chanson (2006). It is also noted that these numerical simulations were completed for a wet bed dam-break wave, which behaves differently to a dry bed dam-break wave (Chanson 2006).

Figure 10(a) outlines the mesh sensitivity testing at WG1 which is located directly behind the swing gate. As can be seen in Figure 10(a), the element size does not influence the water surface elevation at this wave gauge location. Derschum et al. (2018) explain that for the dam-break wave flume at the University of Ottawa, there is a false floor fitted on top of the flume floor which acts like a bottom sill and constricts the flow. There are also two support columns for the swing gate that protrude into the flume that also constrict flow. Stolle et al. (2018b) suggest that the observed wave profile at WG1 is a result of the flow constrictions. Additionally, the step profile of the dam-break wave at WG2 is also a result of the support columns for the swing gate, which caused cross-waves to be generated in the physical model (Stolle et al. 2018b).

Observing Figures 10(b) and 10(c), it can be seen that as the mesh resolution decreases the numerical model converges to the Chanson (2006) solution quicker. However, all resolutions converge to the quasi-steady state solution of Chanson (2006). At WG2 and WG3, the numerical model resulted in water surface elevations that are within the bounds of the experimental data. The bore front arrival times at WG2 and WG3 in the model are 0.88 s and 1.20 s, while the experimental data had arrival times of approximately 0.91 s and 1.39 s respectively. The numerical model resulted in bore fronts that are traveling faster than in the experimental data. This is likely associated with the frictional factor used for the flume bed in the computational domain. A constant value of 0.0293 was applied to the flume bed over the entire computational domain, which is based on the mean frictional factor from Stolle et al. (2019). Further details of the model setup can be found in Joynt et al. (2021).

WG4 is positioned at the face of the structure. As depicted in Figure 10(d), a reduction in element size resulted in a decrease in bore arrival time, and an increase in splash-up magnitude. This suggests that the numerical model's bore front is moving faster than the experimental data. It's worth noting, however, that the numerical model's splash magnitude remains within the experimental data boundaries, and the quasi-steady state flow in the model falls within the upper limits of the experimental data.

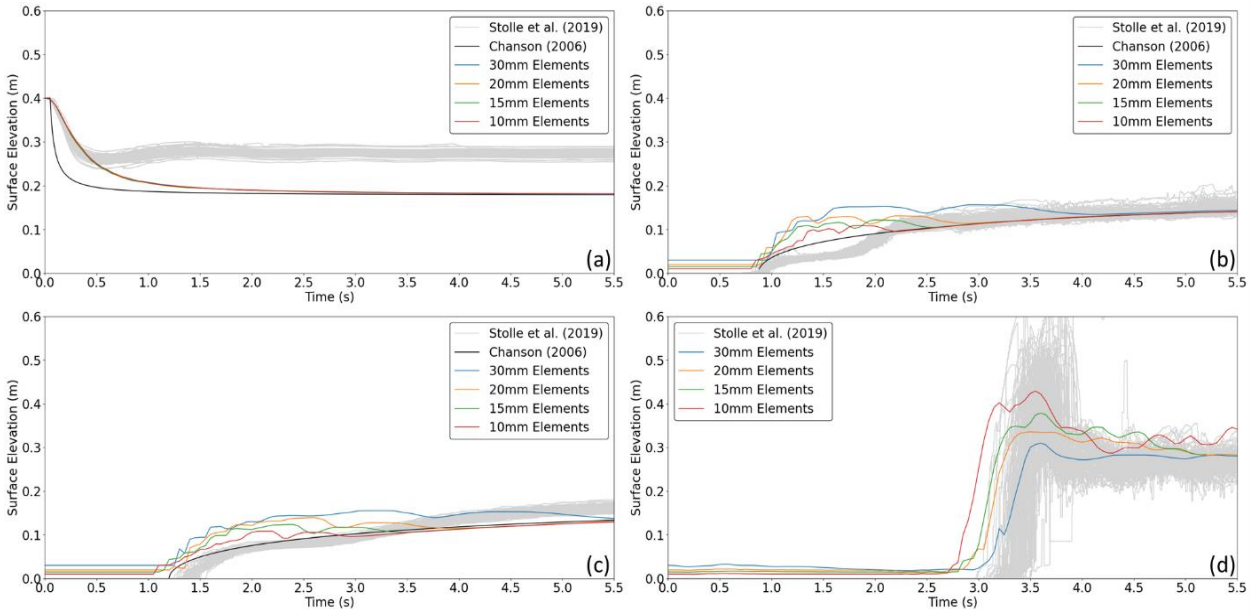

Figure 10: ALE Mesh Sensitivity on Water Surface Elevation – (a) WG1, (b) WG2, (c) WG3, (d) WG4.

Figure 11 outlines the mesh sensitivity of the hydrodynamic force on the structure. The raw numerical data was collected at an output frequency of 100,000 Hz, and a rolling mean was subsequently calculated to represent the data at a frequency of 100 Hz. The solid lines on the graph represent the raw data, while the dashed lines represent the rolling mean. From Figure 11, it is apparent that the model overestimates the experimental data, both at the initial hydrodynamic force and the quasi-steady state force. This result can be expected as the bore front arrives at the structure quicker in the model, meaning the bore front is travelling at a faster velocity than the experimental data which results in a larger force. Furthermore, the bore velocity increased as the element size decreased. This correlates to larger initial hydrodynamic forces being generated as the element size decreased, which is exactly what is seen in Figure 11. The quasi-steady state hydrodynamic force from the model decreased as the element size decreased, with the 10 mm element size providing the closest results to the experimental data.

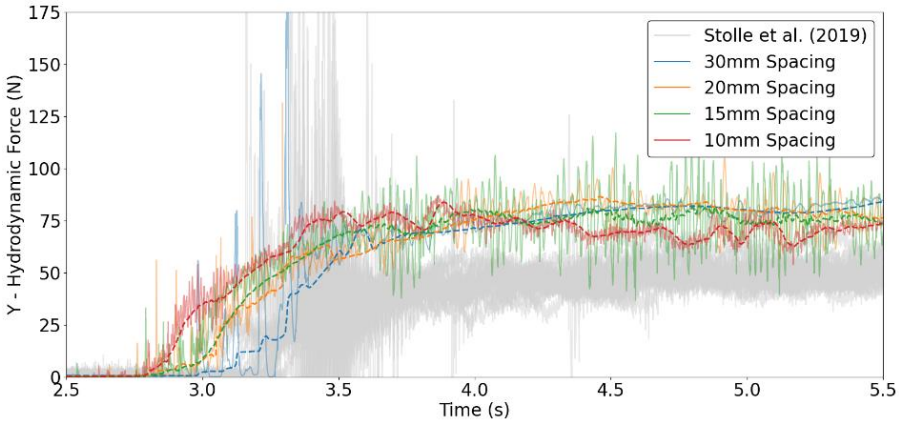

Figure 11: ALE Mesh Sensitivity on Hydrodynamic Force

Based on the results of the mesh sensitivity analysis, a 15 mm mesh size was chosen. The 10 mm solution produced a bore front that arrived earlier than the experimental data, resulting in larger initial hydrodynamic forces. However, the quasi-steady state hydrodynamic forces did not differ significantly between the 10 mm and 15 mm solutions. Additionally, the 10 mm solution required more memory and computational power than the 15 mm solution (Joynt et al. 2021). The 15 mm solution was selected as it better fit the experimental data and the Chanson (2006) solution when compared to the 20 mm and 30 mm solutions and it also did not require a significant amount of additional computational power.

4.2 Results and Discussion

4.2.1 Water Surface Elevations and Hydrodynamic Forces

Figure 12 illustrates the water surface elevations at all wave gauges. The presence of debris did not affect the water surface elevations at WG1, WG2, and WG3 because the debris centroid is located +3.20 m down the flume, while WG1 and WG2 were located at -0.10 m and +2.40 m respectively. Since WG3 was offset to one side of the flume, the debris did not affect it, despite being located at the same coordinate as the debris centroid.

Figure 12(d) shows the water surface elevation at WG4, located at the face of the structure. Observing Figure 12(d) reveals no noticeable increase in water surface disruption as the number of debris increased. This lack of significant disruption can be attributed to the simulation of a maximum of only six debris, which may not be sufficient to cause substantial alterations in the water surface elevations. All water surface elevation profiles fit within the experimental data at WG4.

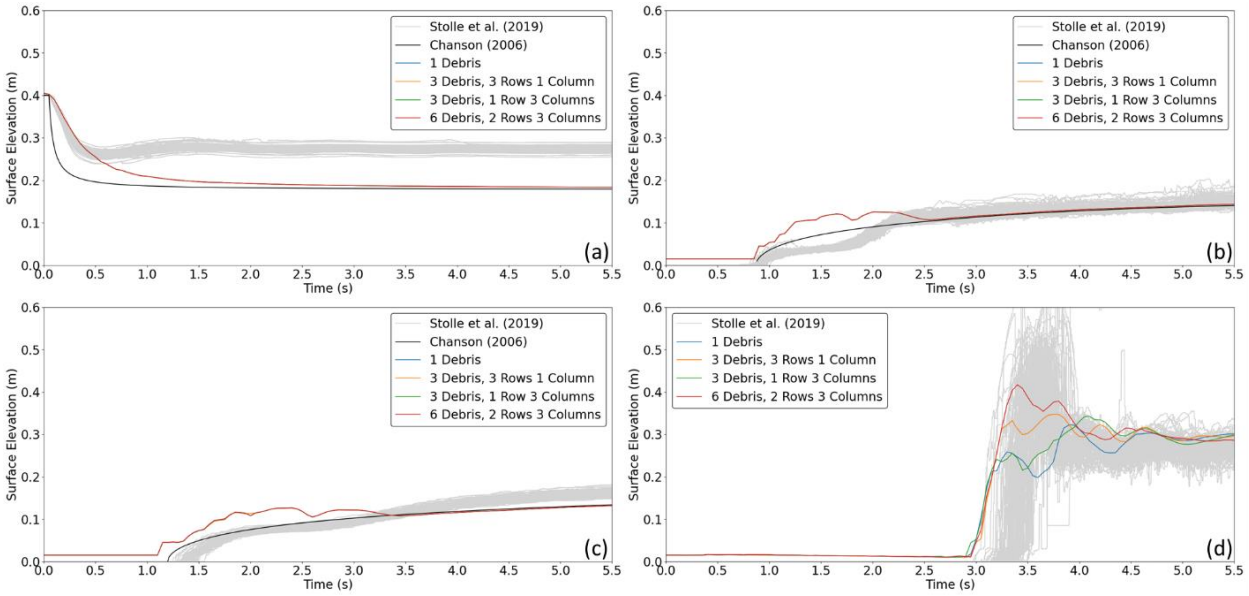

Figure 12: Multi-Debris Simulations – Water Surface Elevation at (a) WG1, (b) WG2, (c) WG3, (d) WG4.

The hydrodynamic force for each simulation is presented in Figure 13. As described for WG4, there is no clear trend associated with the hydrodynamic force and the number of debris being modelled. The hydrodynamic force is directly related to the water surface elevation at the face of the structure presented in Figure 12(d). The hydrodynamic force increased as the water surface elevation at the face of the structure increased.

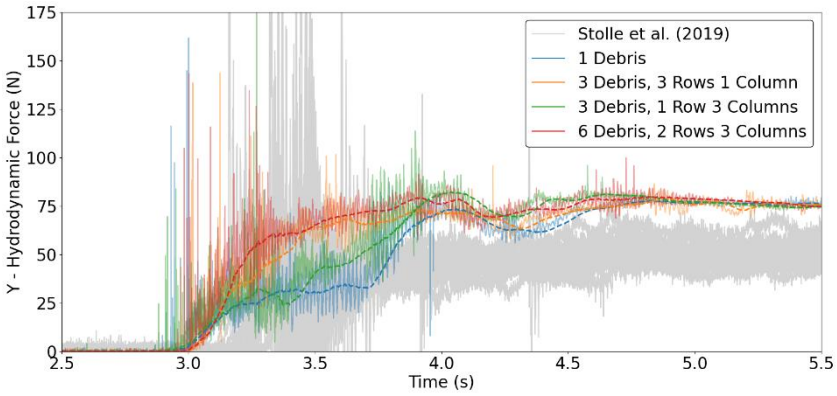

Figure 13: Multi-Debris Simulations – Hydrodynamic Force Timeseries Comparison on the Structure

4.2.2 Debris Transport

Figure 14 illustrates the transport paths (traces) that the center of gravity of the debris followed for all simulations. The potential spreading areas of the debris are also shown in the figure, along with the debris traces from the experimental data from Stolle et al. (2018a). The debris spreading areas outlined by Naito et al. (2014) and Nistor et al. (2017b) were modified as the current definitions start the spreading area at the debris centroid. Following Clause 6.11.5.1 of ASCE 7-22, the modification to the spreading area starts the spreading at a line parallel to the flow that spans the length of the debris source. The starting line is determined by the y-coordinate of the debris centroid that is the furthest upstream from the structure, and the x-coordinates of the debris centroids that are the furthest apart from each other. For these simulations, the y-coordinate was governed by the six debris simulation and the x-coordinate was governed by the three debris simulation using three rows and one column. Using the starting line, the debris spreading area is then defined by the spreading angles outlined by Naito et al. (2014) and Nistor et al. (2017b). As can be seen from Figure 14, this modification to the debris spreading area does capture the debris traces from the simulations with only one debris falling slightly outside of the debris spreading area defined by Nistor et al. (2017b)

It is important to highlight that the experimental data by Stolle et al. (2108a) pertains to single debris transport. Comparing the single debris transport data with the numerical model result, it is evident that the model captures the debris transport well.

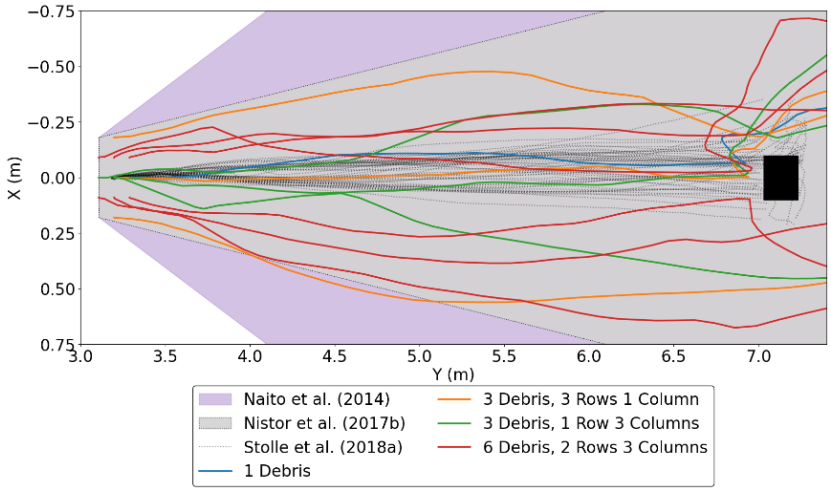

Figure 14: Multi-Debris Simulations – Debris Centroid Transport Path Along the Numerical Flume

4.2.3 Debris Impact Force

Figure 15(a) outlines the debris impact force histories of each simulation. As can be seen from Figure 15, not all of the debris contacted the structure. In the event that more than one debris contacts the structure, the different impact force histories will have the same color, designating them as occurring in the same simulation, however, the line styles will differ.

Figure 15(a) demonstrates that the model resulted in initial debris impact force histories that are similar when compared to the impact force histories developed by the MDOF fitting method described previously. There is one outlier impact history in Figure 15(a) associated with the three debris oriented with three rows and one column simulation. For this simulation, the first impact event results in two impacts with small magnitudes and durations. The negative impact force implies that the debris was transported around to the downstream side of the structure after the initial impact and contacted the structure in the negative y-direction. The small magnitudes and durations are due to the impact event being a glancing impact. Both the six debris simulation and three debris oriented with one row and three columns resulted in secondary impacts due to rebounding off of the structure. The rebounded impact forces were smaller in magnitude but had durations that were not dissimilar to the initial impacts.

Observing Figure 15(b) the debris impact velocities from the model are similar to the experimental data with two outliers. Both outlier impact velocities are associated with glancing impacts against the structure. The glancing impacts occur at a relatively high velocity for the impact forces they generate.

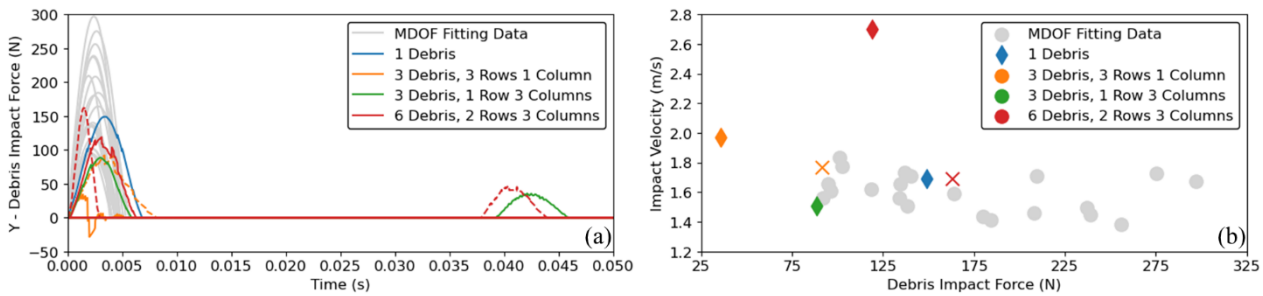

Figure 15: Multi-Debris Simulations – (a) Debris Impact Forces, (b) Initial Debris Impact Velocities

Figure 16 defines the impact orientations of all simulations. The one debris simulation resulted in one impact event and the impact orientation can be seen in Figure 16(a). The debris impacts the structure mostly longitudinally; however, the impact has some degree of obliquity. For the simulation with three debris oriented with three rows and one column, two debris impacted the structure, and the impact orientation is shown in Figure 16(b). Similar to the one debris

simulation, one of the debris impacts the structure longitudinally with some obliquity, while the second debris impact is a glancing impact. The three debris simulation oriented with one row and three columns resulted in one debris impacting the structure twice, the impact orientation is shown in Figure 16(c). Once again, the debris is oriented longitudinally during the impact event. The six debris simulation resulted in two debris impact events, with one of the events striking the structure twice, the orientation of the impacts can be seen in Figure 16(d). Figure 16 illustrates that all the impact events had some degree of obliquity, the impacts were not purely longitudinal impacts on the structure.

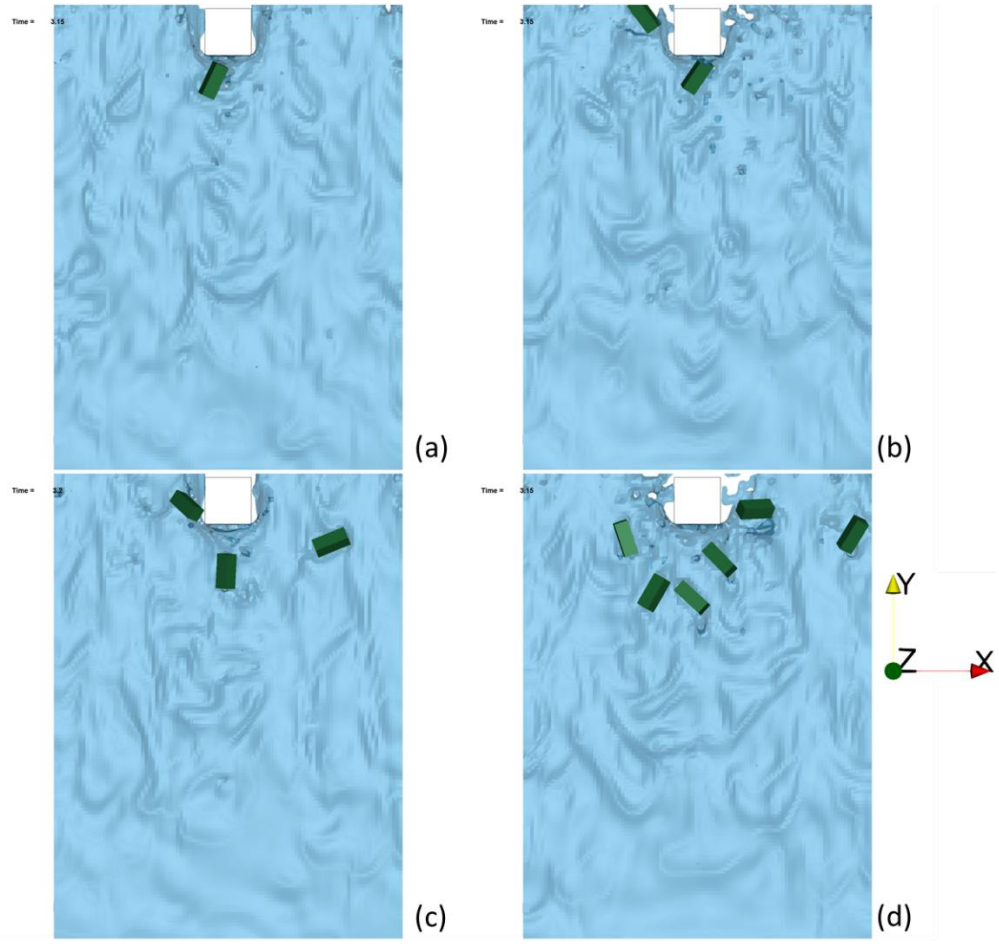

Figure 16: Multi-Debris Simulations – Debris Impact Orientations – (a) 1 Debris, (b) 3 Debris, 3 Rows 1 Column, (c) 3 Debris, 1 Row 3 Columns, (d) 6 Debris, 2 Rows 3 Columns

5 Conclusions

The study presented herein examines alternative methods for calculating debris impact loads and investigated the validity of using SDOF models to predict debris impact forces. The validity of different models to predict debris impact loads was completed by comparing the force response data from experimental data of Stolle et al. (2019) to modelled force response data. Furthermore, a numerical model was developed to simulate single and multi-debris transport and impact loads, which proved to be a reliable tool for estimating debris impact forces.

Throughout this study, the results of using either the structure or debris stiffness to calculate impact loads following Clause 6.11.2 of ASCE 7-22 is presented. The results of the study highlight that the choice of stiffness value used has a significant influence on the impact force histories generated. Sensitivity analysis should be considered by designers when analyzing how structures respond to these types of impact loads.

This study demonstrated that only the MDOF method for estimating debris impact force histories resulted in a response that was in phase and of similar magnitude to the experimental data. The SDOF method and provisions in ASCE 7-22 both resulted in force response that overestimated the magnitude and frequency of the experimental data. Future research

using measured force responses to approximate impact force histories should investigate using a MDOF to back-calculate the impact forces. Additional conclusions regarding the analytical modelling results are as follows:

- Using a SDOF system to estimate an impact force history may provide a response that is in general agreement with the measured data. However, when that same impact force history is applied to a MDOF system, that impact force history no longer results in a realistic force response. It overestimated the forces developed in a structural model.
- As the experimental impact forces increased in magnitude, the validity of using a SDOF model to estimate the debris impact forces decreased.

This study also employed a fully 3D coupled fluid-structure interaction to simulate the debris transport and impact events during dam-break waves. Generally, the study showed that the numerical model was capable of producing similar results to those outlined in Stolle et al (2019) and (2020b) for water surface elevations, hydrodynamic forces, debris transport, and impact forces. However, the numerical modelling results are limited to the experimental results from Stolle et al. (2019) and have not been applied for full-scale flows and debris impact events. Key results from the numerical modelling effort are as follows:

- The numerical model typically overestimated the size of the bore front but converged to the Chanson (2006) solution during steady-state flow. Both solutions (numerical model and Chanson (2006)) fell within the bounds of the experimental data of Stolle et al. (2019). The overestimation is likely due to an overestimation of the downstream water, which is limited to be 1-element size in the numerical model (i.e. 15 mm thick).
- The numerical model resulted in a bore-front that arrived at the structure quicker than in the experimental data of Stolle et al. (2019). This is likely due to the frictional factor applied to the flume bed, which was estimated as 0.0293 in Stolle et al. (2019). A better comparison could have been achieved by further iterating this frictional factor.
- The numerical model resulted in hydrodynamic forces due to the splash up of water at the face of the structure that fell within the bounds of the experimental data of Stolle et al. (2019). However, the quasi-steady state hydrodynamic force from the model overestimated the experimental data, which could be attributed to the bed frictional factor allowing increased velocities.
- The numerical model was capable of simulating multi-debris impact events that resulted in debris transport that fell within the bounds outlined in Naito et al. (2014) and Nistor et al. (2017b), modified by Clause 6.11.5.1 of ASCE 7-22.
- The numerical model resulted in debris impact force histories that compared well to the impact histories developed from the MDOF fitting method. This highlights the potential use of numerical models to simulate these types of events.

Acknowledgements

This study was made possible by the work done by Dr. Jacob Stolle during his PhD, who graciously supplied the measured data used for the basis of this study. Additionally, the authors would like to acknowledge that this research was enabled in part by support provided by Compute Ontario and Compute Canada.

Author contributions (CRediT)

Patrick Joynt: Methodology, Data curation, Formal Analysis, Simulation, Validation, Visualization, Writing-original draft and editing. Ioan Nistor: Methodology, Supervision, Funding, Writing-review and editing. Dan Palermo: Methodology, Supervision, Funding, Writing-review and editing. Jacob Stolle: Data collection and distribution, Writing-review and editing.

Conflict Of Interest (COI)

There is no conflict of interest.

References

Aghl, Payam Piran, Clay J. Naito, and H. Ronald Riggs. 2015. "Estimation of Demands Resulting from Inelastic Axial Impact of Steel Debris." *Engineering Structures* 82: 11-21.

Aghl, Payam Piran, Clay J. Naito, and H. Ronald Riggs. 2014. "Full-Scale Experimental Study of Impact Demands Resulting from High Mass, Low Velocity Debris." *Journal of Structural Engineering* 140 (5).

ANSYS. 2018. "Ansys Granta Design Sample Materials. Version 19.1."

ASCE 7. 2022. *Minimum Design Loads and Associated Criteria for Buildings and Other Structures.* American Society of Civil Engineers.

Chanson, Hubert. 2006. "Tsunami Surges on Dry Coastal Plains: Application of Dam Break Wave Equations." *Coastal Engineering Journal* (Taylor & Francis) 48: 335-370.

Chopra, Anil k. 2017. *Dynamics of Structures: Theory and Applications to Earthquake Engineering.* Pearson.

Derschum, C., I. Nistor, J. Stolle, and N. Goseberg. 2018. "Debris impact under extreme hydrodynamic conditions part 1 : Hydrodynamics and impact geometry." *Coastal Engineering* 141: 24-35.

Haehnel, Robert B, and Steven F Daly. 2004. "Maximum Impact Force of Woody Debris on Floodplain Structures." *Journal of Hydraulic Engineering* 130 (2): 112 - 120.

Hallquist, John O. 2006. *LS-DYNA Theory Manual.* Livermore Software Technology Corporation.

Huang, Norden E, Zheng Shen, Steven R Long, Manli C Wu, Hsing H Shih, Quanan Zheng, Nai-Chyuan Yen, Chi Chao Tung, and Henry H Liu. 1998. "The empirical mode decomposition and the Hilbert spectrum for nonlinear and non-stationary time series analysis." *Proceedings of the Royal Society. A, Mathematical, physical, and engineering sciences* 454 (1971): 903-995.

Ikeno, Masaaki, Daisuke Takabatake, Naoto Kihara, Hideki Kaida, Yoshinori Miyagawa, and Atsushi Shibayama. 2016. "Improvement of Collision Force Formula for Woody Debris by Airborne and Hydraulic Experiments." *Coastal Engineering Journal* 58 (4): 1-23.

Ikeno, Masaaki, Naoto Kihara, and Daisuke Takabatake. 2013. "Simple and Practical Estimation of Movement Possibility and Collision Force of Debris due to Tsunami." *Journal of Japan Society of Civil Engineers* 69: 861-865.

Joynt, Patrick, Ioan Nistor, and Dan Palermo. 2021. *Flood-Entrained Debris Impacts on Structures : A Structural-Hydraulic Numerical Analysis.* Ottawa: Université d'Ottawa / University of Ottawa. doi:http://dx.doi.org/10.20381/ruor-25970.

Khowitar, Eid, H. Ronald Riggs, and Marcelo H. Kobayashi. 2014. "Beam Response to Longitudinal Impact by a Pole." *Journal of Engineering Mechanics* 140 (7).

Ko, H. T.-S., D. T Cox, H. Ronald Riggs, and Clay J. Naito. 2015. "Hydraulic Experiments on Impact Forces from Tsunami-Driven Debris." *Journal of Waterway, Port, Coastal, and Ocean Engineering* 141 (3).

Matsutomi, Hideo. 2009. "Method for Estimating Collision Force of Driftwood Accompanying Tsunami Inundation Flow." *Journal of Disaster Research* 4 (6).

Naito, Clay, Christina Cercone, H. R. Riggs, and Daniel Cox. 2014. "Procedure for Site Assessment of the Potential for Tsunami Debris Impact." *Journal of Waterway, Port, Coastal and Ocean Engineering* 140 (2): 223-232.

Navaratnam, Christy Ushanth, Alf Torum, and Oivind A. Arntsen. 2013. "Preliminary Analysis of Wave Slamming Force Response Data from Tests on a Truss Structure in Large Wave Flume, Hannover, Germany."

Nistor, Ioan, Nils Goseberg, and Jacob Stolle. 2017. "Tsunami-Driven Debris Motion and Loads: A Critical Review." *Frontiers in Built Environment* 3.

Nistor, Ioan, Nils Goseberg, Jacob Stolle, Takahito Mikami, Tomoya Shibayama, Ryota Nakamura, and Shunya Matsuba. 2017. "Experimental Investigations of Debris Dynamics over a Horizontal Plane." *Journal of Waterway, Port, Coastal, and Ocean Engineering* 143.

Oumeraci, H., H. W. Partenscky, S. Kohlhase, and P. Klammer. 1993. "Impact Loading and Dynamic Response of Caisson Breakwaters Results of Large-Scale Model Tests." *Coastal Engineering* 1475-1488.

Palermo, Dan, Ioan Nistor, T Al-Faesly, and A. Cornett. 2012. "Impact of Tsunami Forces on Structures: The University of Ottawa Experience." *Proceedings of the Fifth International Tsunami Symposium, Ispra, Italy.*

Riggs, H. Ronald, Marcelo H. Kobayashi, D. T. Cox, Payam Piran Aghl, Eid Khowitar, Clay J. Naito, and H. T.-S. Ko. 2013. "Water-Driven Debris Impact Forces on Structures: Experimental and Theoretical Program." *ASME 2013 32nd International Conference on Ocean, Offshore and Arctic Engineering.*

Stolle, J, C Krautwald, I Robertson, H Achiari, T Mikami, R Nakamura, T Takabatake, et al. 2020. "Engineering Lessons From the 28 September 2018 Indonesian Tsunami: Debris Loading." *Canadian Journal of Civil Engineering* (NRC Research Pres) 47: 1-12.

Stolle, J., C. Derschum, N. Goseberg, I. Nistor, and Emil Petriu. 2018b. "Debris impact under extreme hydrodynamic conditions part 2 : Impact force responses for non-rigid debris collisions." *Coastal Engineering* 141: 107-118.

Stolle, Jacob, Ioan Nistor, Nils Goseberg, and Emil Petriu. 2020. "Multiple Debris Impact Loads in Extreme Hydrodynamic Conditions." *Journal of Waterway, Port, Coastal, and Ocean Engineering* 146 (2).

Stolle, Jacob, Nils Goseberg, Ioan Nistor, and Emil Petriu. 2019. "Debris impact forces on flexible structures in extreme hydrodynamic conditions." *Journal of Fluids and Structures* 84: 391-407.

Stolle, Jacob, Nils Goseberg, Ioan Nistor, and Emil Petriu. 2018a. "Probabilistic Investigation and Risk Assessment of Debris Transport in Extreme Hydrodynamic Conditions." *Journal of waterway, port, coastal, and ocean engineering* (American Society of Civil Engineers) 144.

Syamsidik, Benazir, Muksin Umar, Giordano Margaglio, and Afri Fitrayansyah. 2019. "Post-Tsunami Survey of the 28 September 2018 Tsunami near Palu Bay in Central Sulawesi, Indonesia: Impacts and Challenges to Coastal Communities." *International Journal of Disaster Risk Reduction* 38: 110-132.